J. Fluid Mech. (1988), *vol.* 190, *pp.* 299–319
Printed in Great Britain

The axisymmetric rise of a spherical bubble at the exit of an orifice in the presence of a stagnant cap of insoluble surfactants

By ZEEV DAGAN†, ZONG-YI YAN‡ AND HUIXIAN SHEN‖

† Department of Mechanical Engineering, The City College of the City University of New York, New York, NY 10031, USA

‡ Department of Mechanics, Peking University, Beijing, China

‖ Department of Mathematics, The Affiliated College of Peking University, Beijing, China

(Received 2 January 1987 and in revised form 21 October 1987)

The motion of a spherical droplet in unbounded exterior phase in the presence of a stagnant cap of adsorbed insoluble surfactants has been recently presented by Sadhal & Johnson (1983). The present study considers the axisymmetric motion of a gas bubble at the exit of a circular orifice in the presence of a similar stagnant cap.

The solution procedure utilizes the boundary integral representation in order to obtain the drag correction factor for a bubble translating away from the orifice in otherwise quiescent fluid, and for a fixed bubble exposed to Sampson's flow towards the orifice. It is demonstrated that the presence of the confining orifice boundaries substantially increases the drag acting on the bubble, and the solution approaches the exact result of Sadhal and Johnson as the distance between the bubble and the orifice is increased. Furthermore, it is shown that for a fixed amount of surfactants on the bubble surface the cap angle increases with distance from the orifice due to the diminishing hydrodynamic interaction. Hence, the quasi-steady terminal velocity of a bubble rising from an orifice is reduced by the viscous boundary interaction, and by the growing immobile cap size.

1. Introduction

Heat and mass transfer processes involving drops are common in many engineering applications. Some salient examples include chemical extraction equipment and direct-contact heat exchangers, where it is essential to determine the droplet residence time in the transfer chamber and the effectiveness of the transport between the two fluid phases (Hetsroni 1982). The major factors that can significantly alter the transport efficiency in such systems are the transfer enhancement by the external convection and internal circulation, and motion retardation by interfacial Marangoni forces. The convective enhancement is, however, extremely sensitive to decreasing drop size owing to increasing influence of the surface-active material which is commonly present on interfaces between two immiscible fluids. The presence of surfactant on the interface between the droplet and the exterior liquid can act to suppress the internal circulation (Savic 1953) by forming a stagnant cap on the trailing surface of the droplet (Griffith 1962).

The mechanism responsible for the reduction of the droplet terminal velocity and surface mobility by surfactants was first elucidated by Levich (1962). Interfacial

tension variation arising from non-uniform distribution of surfactant molecules (Marangoni effect) will lower the surface tension on the downstream droplet surface where surfactant concentration is larger owing to the accumulation by the sweeping external flow (Johns & Beckman 1966). Consequently, a surface-tension gradient is established over the droplet surface which acts in the direction of the front stagnation point and opposes the hydrodynamic stress exerted by the external flow. The purpose of the present study is to examine the additional effect of the viscous hydrodynamic interaction on the motion of a bubble in the vicinity of a circular orifice in the presence of insoluble surfactants.

In general, the hydrodynamic and mass-transfer-field equations that govern the motion of a droplet in another liquid are coupled. The coupling is manifested by the tangential stress balance on the surface of the droplet, the surface convective diffusion equation for the surfactant concentration, and the bulk-solute convective diffusion equation in both phases. Surfactant present in the bulk phase can be transferred to the vicinity of the droplet surface by either convective or molecular diffusion and, thereafter, adsorb to it. Levich (1962) distinguished between two cases in which the flux of the surface-active material on to the droplet surface is controlled by the slower of the following steps: (i) adsorption or desorption; (ii) bulk diffusion. In the first case, the effect of the surfactant on the interfacial velocity is more pronounced than that due to solute transfer. Hence, the latters influence can be neglected, and the flow-field equations can be solved independently from the bulk mass-transfer equations. In the second case, when the surfactant transfer is the rate-limiting step (the surface is assumed to be in adsorption equilibrium with the local concentration in the bulk phase), the surface convective diffusion equation for the concentration of the adsorbed substance is coupled with the hydrodynamic equation by the tangential-stress-balance requirement, and the diffusional flux from the bulk to the surface represents the coupling between the interfacial equation and the bulk transport equations. A third possible limiting case is that of the surfactant being insoluble. Then, a vanishing flux of the surfactant to the droplet surface is assumed and the Marangoni phenomenon is controlled by surfactant transport along the interface due to convection and surface diffusion.

All previous theoretical studies have considered the motion of a droplet in unbounded flow under various limiting assumptions which are useful mathematically for the uncoupling of the governing field equations. Wasserman & Slattery (1969) introduced a perturbation solution for the Hadamard Rybczynski velocity field when a small quantity of surfactant is present in the exterior liquid. Several modifications of the analysis have been carried out by Saville (1973), Harper (1974) and Leven & Newman (1976). The influence of surface shear and surface dilatational viscosities was incorporated in the analysis by Argawal & Wasan (1979) who extended Saville's (1973) boundary-layer approximation for the diffusion of surfactants to the droplet interface. Other perturbation analyses, based on Levich's treatment of the problem, considered small deviation of the surfactant concentration from the equilibrium level (Schechter & Farely 1963; Newman 1967), which represents uniform retardation of the interfacial velocity, and is suitable for large surface-diffusion coefficient (small Péclet number) with non-vanishing velocity over the entire droplet surface.

Experimental observations of droplets of small and moderate size in liquids contaminated by surfactant have indicated, however, that the interfacial velocity is not reduced uniformly, but that a stagnant cap is formed at the rear of the drop (Savic 1953; Garner & Skelland 1955; Griffith 1962; Horton, Fritsch & Kintner 1965;

Huang & Kintner 1969; Beitel & Heideger 1971). The mathematical difficulty in treating this problem arises from the fact that the boundary conditions on the droplet surface are mixed owing to the immobile cap surface. Several approaches had been partially successful (Davis & Acrivos 1966; Harper 1973, 1982) before Sadhal & Johnson (1983) obtained the exact solution to the problem provided that the cap angle is specified, based on Collins (1961) analysis of dual series equations.

In all cases discussed above, the unbounded problem has been examined (an extensive summary of the various possibilities has been presented by Holbrook & Levan 1983*a*, *b*). Nevertheless, the influence of confining boundaries on the droplet velocity and surfactant cap angle has not been considered. This paper presents the first solution, using the integral method, for the problem of a bubble rising from an orifice in the presence of an immobile cap.

2. Mathematical formulation

The system under consideration consists of a gas bubble of radius a' translating axisymmetrically with velocity U' away from an orifice of radius b' (figure 1), in viscous incompressible fluid of viscosity μ and density ρ. The interfacial tension is assumed to be sufficiently large so as to maintain a spherical bubble shape.

In the limit of low Reynolds number and high Péclet number the hydrodynamic governing equations are

$$\frac{\partial V_i}{\partial x_i} = 0, \tag{2.1}$$

$$\frac{\partial^2 V_i}{\partial x_j \partial x_j} = \frac{\partial P}{\partial x_i}, \tag{2.2}$$

and the interfacial surfactant transport equation is

$$\frac{\partial (\Gamma V_s)}{\partial x_s} = 0. \tag{2.3}$$

Here, V_i is the velocity vector, P is the pressure, Γ is the concentration of the surface-active substance and the subscript s denotes the interfacial phase. The variables in the above equations are made dimensionless by using the bubble radius as a lengthscale, a characteristic velocity U_0, which is conveniently defined later, and the stress (or pressure) scale $\mu U_0/a'$. The surface concentration is scaled by the maximum value of Γ at $\theta = 0$.

Following Sadhal & Johnson (1983), integration of (2.3) in spherical coordinates yields the result

$$\Gamma V_s = A/\sin\theta, \tag{2.4}$$

where A is a constant, which must be zero in order for the solution to be bounded at $\theta = 0$ and $\theta = \pi$. Therefore, an immobile surfactant cap must be present on the interface such that

$$V_s = 0 \quad \text{for } 0 \leqslant \theta \leqslant \gamma, \tag{2.5a}$$

where $\Gamma \neq 0$, and the remaining surface is mobile ($V_s \neq 0$) provided

$$\Gamma = 0 \quad \text{for } \gamma \leqslant \theta \leqslant \pi. \tag{2.5b}$$

Consequently, the immobile-cap formation on the bubble surface, described by (2.5), introduces mixed hydrodynamic boundary conditions that must be satisfied on the interface. Choosing spherical coordinates (r, θ, ϕ) at the bubble centre, and cylindrical

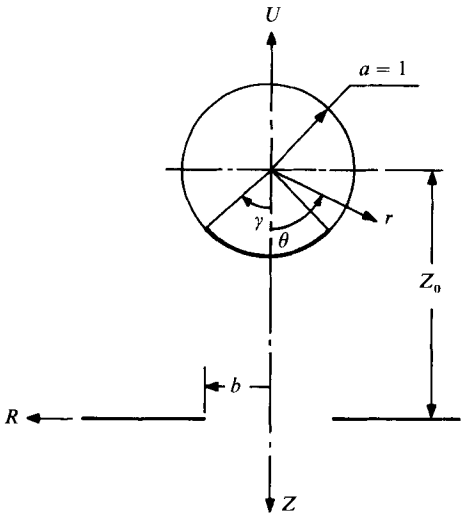

FIGURE 1. System geometry (the stagnant cap is denoted by the heavy line).

coordinates $(R, \tilde{\theta}, Z)$ at the orifice centre, the boundary conditions can be written as follows:

$$V_i(\boldsymbol{x}) = -U\boldsymbol{k} \qquad \text{when } \boldsymbol{x} \in S_b^{(1)} \quad (r = 1, \quad 0 \leqslant \theta \leqslant \gamma), \tag{2.6a}$$

$$V_r = -U\cos\theta, \quad \tau_{r\theta}(\boldsymbol{x}) = 0 \quad \text{when } \boldsymbol{x} \in S_b^{(2)} \quad (r = 1, \quad \gamma \leqslant \theta \leqslant \pi), \tag{2.6b}$$

where V_r is the radial velocity component, $\tau_{r\theta}$ is the tangential stress, $\boldsymbol{x}$ is the position vector and $\boldsymbol{k}$ is the unit vector in the Z-direction. The additional no-slip condition on the orifice wall requires that

$$V_i(\boldsymbol{x}) = 0 \quad \text{when } \boldsymbol{x} \in S_w \quad (Z = 0, \quad R \geqslant b). \tag{2.6c}$$

while far from the orifice, when $(R^2 + Z^2)^{\frac{1}{2}} \to \infty$, the pressure is prescribed by

$$P = P_{\pm\infty} \quad \text{for } Z \lessgtr 0 \tag{2.6d}$$

and the velocity must vanish, $V_i(\boldsymbol{x}) = 0$. The system boundaries in (2.6) are denoted by $S_b^{(1)}$ for the stagnant cap, $S_b^{(2)}$ for the clean bubble surface and S_w for the orifice wall with $S_{w^\pm}$ denoting the two sides of the wall as $Z \to 0^\pm$ respectively.

The solution of the governing equations (2.1) and (2.2), subject to the boundary conditions (2.6), is now presented in terms of the integral method described by Yan *et al.* (1986). In principle, it can be solved by the multipole collocation technique, which was used by Dagan, Weinbaum & Pfeffer (1982) for the axisymmetric motion of a solid sphere towards an orifice. However, in the presence of a stagnant cap the truncated series converges very slowly owing to the discontinuity of the interfacial velocity, as demonstrated by Davis & Acrivos (1966) for the motion of a similar bubble in unbounded flow. Following the procedure of Yan *et al.* (1986), the fluid velocity is decomposed into two distinct contributions: the Sampson solution $V_i^s(\boldsymbol{x})$ for the flow through an orifice in the absence of the bubble; and the disturbance $V_i'(\boldsymbol{x})$, which can be represented in terms of the hydrodynamic potentials generated by the distribution of singularities over all the boundaries. Hence,

$$V_i(\boldsymbol{x}) = V_i^s(\boldsymbol{x}) + V_i'(\boldsymbol{x}), \tag{2.7a}$$

and the corresponding pressure field is decomposed as follows:

$$P(\boldsymbol{x}) = P^{\mathrm{s}}(\boldsymbol{x}) + P'(\boldsymbol{x}), \tag{2.7b}$$

where the Sampson solution is given by (Happel & Brenner 1973, p. 153)

$$V_R^{\mathrm{s}} = -\frac{3q}{8\pi b^2} Z \frac{\zeta}{R} (R_1 - R_2)\left(\frac{1}{R_1} - \frac{1}{R_2}\right), \tag{2.8a}$$

$$V_Z^{\mathrm{s}} = \frac{3q\zeta}{8\pi R b^2} (R_1 - R_2)\left(\frac{R-b}{R_1} - \frac{R+b}{R_2}\right), \tag{2.8b}$$

$$P^{\mathrm{s}} = \frac{3q}{\pi b^3}\left(\frac{\lambda}{\lambda^2+\zeta^2} + \tan^{-1}\lambda\right), \tag{2.8c}$$

where

$$q = \tfrac{1}{3} b^3 (P_{-\infty} - P_{+\infty}), \quad \lambda = \left[\left(\frac{R_1+R_2}{2b}\right)^2 - 1\right]^{\frac{1}{2}}, \tag{2.9a,b}$$

$$\zeta = \left[1 - \left(\frac{R_1 - R_2}{2b}\right)^2\right]^{\frac{1}{2}}, \quad R_{2,1} = [Z^2 + (R \pm b)^2]^{\frac{1}{2}}. \tag{2.9c,d}$$

Here, q is the dimensionless volume flux and (λ, ζ) are oblate spheroidal coordinates.

2.1. *Integral representation*

The Green's formula for low-Reynolds-number flow was first derived by Ladyzhenskaya (1963) in the form

$$\int_\Omega \left\{ V_i(\boldsymbol{y}) \left[\frac{\partial^2 u_i}{\partial y_j \partial y_j}(\boldsymbol{x},\boldsymbol{y}) - \frac{\partial p^k}{\partial y_i}(\boldsymbol{y},\boldsymbol{x})\right] - u_i^k(\boldsymbol{x},\boldsymbol{y}) \left[\frac{\partial^2 V_i}{\partial y_j \partial y_j}(\boldsymbol{y}) - \frac{\partial P}{\partial y_i}(\boldsymbol{y})\right]\right\} \mathrm{d}\Omega_y$$
$$= \int_{\partial\Omega} \{V_i(\boldsymbol{y}) T_{ij}[\boldsymbol{u}^k(\boldsymbol{x},\boldsymbol{y})]\, n_j(\boldsymbol{y}) - u_i^k(\boldsymbol{x},\boldsymbol{y}) T_{ij}[\boldsymbol{V}(\boldsymbol{y})]\, n_j(\boldsymbol{y})\}\, \mathrm{d}S_y, \tag{2.10}$$

where V_i and P are the solutions of (2.1) and u_i^k and p^k are the solution at point $\boldsymbol{x}$ due to a Stokeslet in the kth direction at point $\boldsymbol{y}$. The latter are given by

$$u_i^k(\boldsymbol{x},\boldsymbol{y}) = -\frac{1}{8\pi}\left[\frac{\delta_{ij}}{r_{xy}} + \frac{(x_i - y_i)(x_k - y_k)}{r_{xy}^3}\right], \tag{2.11a}$$

$$p^k(\boldsymbol{x},\boldsymbol{y}) = \frac{y_k - x_k}{4\pi r_{xy}^3}, \tag{2.11b}$$

where $r_{xy} = |\boldsymbol{x} - \boldsymbol{y}|$ and δ_{ij} is the Kronecker delta. Finally, T_{ij} represents the stress tensor associated with the two velocity fields, namely

$$T_{ij}[\boldsymbol{V}(\boldsymbol{y})] = -\delta_{ij} P(\boldsymbol{y}) + \frac{\partial V_i}{\partial y_j}(\boldsymbol{y}) + \frac{\partial V_j}{\partial y_i}(\boldsymbol{y}), \tag{2.12a}$$

$$T_{ij}[\boldsymbol{u}^k(\boldsymbol{x},\boldsymbol{y})] = -\delta_{ij} p^k(\boldsymbol{y},\boldsymbol{x}) + \frac{\partial u_i^k}{\partial y_j}(\boldsymbol{x},\boldsymbol{y}) + \frac{\partial u_j^k}{\partial y_i}(\boldsymbol{x},\boldsymbol{y}). \tag{2.12b}$$

Here, n_j is the exterior unit vector to the boundaries $\partial\Omega$ of the flow domain Ω, and the subscript y in $\mathrm{d}S_y$ and $\mathrm{d}\Omega_y$ indicates integration over $\boldsymbol{y}$.

Using the Green's formula the velocity field $\boldsymbol{V}(\boldsymbol{x})$ can be represented in terms of the single and double layer potentials $V_i^{(1)}$ and $V_i^{(2)}$ respectively:

$$V_i(\boldsymbol{x}) = V_i^{(1)}(\boldsymbol{x}) + V_i^{(2)}(\boldsymbol{x}), \tag{2.13a}$$

where

$$V_i^{(1)}(\boldsymbol{x}) = -\int_{\partial\Omega} u_i^k(\boldsymbol{x},\boldsymbol{y})\, T_{kj}[\boldsymbol{V}(\boldsymbol{y})]\, n_j(\boldsymbol{y})\, \mathrm{d}S_y, \tag{2.13b}$$

$$V_i^{(2)}(\boldsymbol{x}) = \int_{\partial\Omega} T_{ij}[\boldsymbol{u}^k(\boldsymbol{x},\boldsymbol{y})]\, V_k(\boldsymbol{y})\, n_j(\boldsymbol{y})\, \mathrm{d}S_y. \tag{2.13c}$$

The general representation (2.13) is valid if both the velocity $\boldsymbol{V}(\boldsymbol{x})$ and the pressure $P(\boldsymbol{x})$ vanish at infinity. Hence, it cannot be directly applied to the present system where $P_{-\infty} \geqslant P_{\infty}$. Nevertheless, this restriction can be eliminated by using the decomposition (2.7) whereby the disturbance fields $\boldsymbol{V}'(\boldsymbol{x})$ and $P'(\boldsymbol{x})$ vanish at infinity. Furthermore, for a Lyapunov surface, the single layer potential $V_i^{(1)}(\boldsymbol{x})$ is continuous but the double layer potential $V_i^{(2)}(\boldsymbol{x})$ is discontinuous across $\partial\Omega$ and is given by

$$\lim_{\boldsymbol{x}\to\boldsymbol{x}_0} V_i^{(2)}(\boldsymbol{x}) = V_i^{(2)}(\boldsymbol{x}_0) + \tfrac{1}{2}V_i(\boldsymbol{x}_0) \quad \text{when } \boldsymbol{x}_0 \in \Omega, \quad \boldsymbol{x}_0 \in \partial\Omega, \tag{2.14}$$

where the factor $\frac{1}{2}$ applies only for continuous surfaces. Since the infinite wall with the orifice is not a Lyapunov surface (has no definite tangent at the edge of the orifice) the Green's formula (2.10) is not directly applicable. Therefore, the flow field shown in figure 1 is divided into two semi-infinite regions separated by the orifice wall such that the boundary of each region consists of Lyapunov surfaces. Consequently, Green's formula can be applied for the disturbance field in each region and the summation of the two expressions yields

$$\begin{aligned} \boldsymbol{V}'(\boldsymbol{x}) = {} & \frac{1}{8\pi}\int_{S_\mathrm{b}} \left[\frac{\delta_{ik}}{r_{xy}} + \frac{(x_i - y_i)(x_k - y_k)}{r_{xy}^3}\right] f_k^{(\mathrm{b})}(\boldsymbol{y})\, \mathrm{d}S_y \\ & - \frac{3}{4\pi}\int_{S_\mathrm{b}} \left[\frac{(x_i - y_i)(x_j - y_j)(x_k - y_k)}{r_{xy}^5}\right] V_k'(\boldsymbol{y})\, n_j(\boldsymbol{y})\, \mathrm{d}S_y \\ & + \frac{1}{8\pi}\int_{S_{\mathrm{w}^-}} \left[\frac{\delta_{ik}}{r_{xy}} + \frac{(x_i - y_i)(x_k - y_k)}{r_{xy}^3}\right] f_k^{(\mathrm{w})}(\boldsymbol{y})\, \mathrm{d}S_y, \end{aligned} \tag{2.15}$$

where S_b denotes the bubble surface and S_{w^-} denotes the planar wall on the bubble side. The density function $f_k(\boldsymbol{y})$ represents the stress difference across each boundary, namely

$$f_k^{(\mathrm{b})}(\boldsymbol{y}) = T_{kj}^{(\mathrm{b})}[\boldsymbol{V}'(\boldsymbol{y})] = -T_{kr}^{(\mathrm{b})}[\boldsymbol{V}'(\boldsymbol{y})], \tag{2.16a}$$

$$f_k^{(\mathrm{w})}(\boldsymbol{y}) = T_{k3}^{(-)}[\boldsymbol{V}'(\boldsymbol{y})] - T_{k3}^{(+)}[\boldsymbol{V}'(\boldsymbol{y})], \tag{2.16b}$$

where $k = 1, 2, 3$, and the superscripts (b), $(-)$ and $(+)$ denote $S^{(\mathrm{b})}$, S_{w^-} and S_{w^+}, respectively. It is important to emphasize that the double layer potential does not contribute to the integral representation (2.15) because $V_k'(\boldsymbol{y}) = 0$ on S_{w^-}. Furthermore, the first two integral terms in (2.15) are evaluated on the bubble surface where mixed boundary conditions are prescribed according to (2.6). Finally, (2.15) is valid for any point $\boldsymbol{x}$ in the flow field and there is no geometrical restriction on the position of the bubble even if it is partially inside the orifice. Still, the latter configuration is excluded from the present analysis because under such conditions bubble deformation is significant.

Using (2.15) in the application of the boundary conditions (2.6) with the discontinuity condition (2.14) yields the following integral equations:

$$-\int_{S_b^{(1)}} u_i^k(\boldsymbol{x},\boldsymbol{y}) f_k^{(b)}(\boldsymbol{y})\,dS_y + \int_{S_b^{(2)}} u_i^k(\boldsymbol{x},\boldsymbol{y}) T_{kr}^{(b)}[V'(\boldsymbol{y})]\,dS_y$$
$$-\int_{S_b^{(2)}} T_{ij}[u^k(\boldsymbol{x},\boldsymbol{y})]\,V_k'(\boldsymbol{y})\,y_j\,dS_y - \int_{S_w^-} u_i^k(\boldsymbol{x},\boldsymbol{y}) f_k^{(w)}(\boldsymbol{y})\,dS_y$$
$$= \tfrac{1}{2}W_i(\boldsymbol{x}) + \int_{S_b^{(1)}} T_{ij}[u^k(\boldsymbol{x},\boldsymbol{y})]\,W_k(\boldsymbol{y})\,y_j\,dS_y, \quad \boldsymbol{x}\in S_b^{(1)}; \quad (2.17a)$$

$$-\tfrac{1}{2}V_i'(\boldsymbol{x}) - \int_{S_b^{(1)}} u_i^k(\boldsymbol{x},\boldsymbol{y}) f_k^{(b)}(\boldsymbol{y})\,dS_y + \int_{S_b^{(2)}} u_i^k(\boldsymbol{x},\boldsymbol{y}) T_{kr}^{(b)}[V'(\boldsymbol{y})]\,dS_y$$
$$-\int_{S_b^{(2)}} T_{ij}[u^k(\boldsymbol{x},\boldsymbol{y})]\,V_k'(\boldsymbol{y})\,y_j\,dS_y - \int_{S_w^-} u_i^k(\boldsymbol{x},\boldsymbol{y}) f_k^{(w)}(\boldsymbol{y})\,dS_y$$
$$= \int_{S_b^{(1)}} T_{ij}[u^k(\boldsymbol{x},\boldsymbol{y})]\,W_k(\boldsymbol{y})\,y_j\,dS_y, \quad \boldsymbol{x}\in S_b^{(2)}; \quad (2.17b)$$

$$-\int_{S_b^{(1)}} u_i^k(\boldsymbol{x},\boldsymbol{y}) f_k^{(b)}(\boldsymbol{y})\,dS_y + \int_{S_b^{(2)}} u_i^k(\boldsymbol{x},\boldsymbol{y}) T_{kr}^{(b)}[V'(\boldsymbol{y})\,dS_y$$
$$-\int_{S_b^{(2)}} T_{ij}[u^k(\boldsymbol{x},\boldsymbol{y})]\,V_k'(\boldsymbol{y})\,y_j\,dS_y - \int_{S_w^-} u_i^k(\boldsymbol{x},\boldsymbol{y}) f_k^{(w)}(\boldsymbol{y})\,dS_y$$
$$= \int_{S_b^{(1)}} T_{ij}[u^k(\boldsymbol{x},\boldsymbol{y})]\,W_k(\boldsymbol{y})\,y_j\,dS_y, \quad \boldsymbol{x}\in S_w^-, \quad (2.17c)$$

where
$$W_k(\boldsymbol{y}) = U_k - V_k^s(\boldsymbol{y}) \quad (2.18)$$

and $U_k = 0$ for $k = 1$ or 2, while $U_3 = -U$. The above equations have to be satisfied for $i = 1$ and $i = 3$ with $\theta = 0$ because of the axial symmetry of the geometry.

2.2. *Numerical collocation technique*

Owing to the axisymmetry of the present system the boundary conditions will be applied at discrete points on the bubble surface and the orifice wall in the same meridian plane. The choice of the collocation points is different for each surface. For the solid cap region on the bubble surface, $S_b^{(1)}$, L points are chosen such that $\theta_1 = \delta$, $\theta_L = \gamma$, and the remaining points are given by

$$\left.\begin{aligned} \theta_i = \frac{i-3}{L-3}\gamma \quad (i = 4,5,\ldots,L-3); \quad \theta_3 = \tfrac{1}{3}(2\theta_1+\theta_4); \quad \theta_2 = \tfrac{1}{3}(2\theta_1+\theta_3); \\ \theta_{L-2} = \tfrac{1}{3}(2\gamma+\theta_{L-3}); \quad \theta_{L-1} = (2\gamma+\theta_{L-2}), \end{aligned}\right\} \quad (2.19a)$$

where δ is a small positive number (chosen as 0.01). Similarly, on the clean interface of the bubble, $S_b^{(2)}$, M points are selected such that $\theta_1' = \gamma$, $\theta_M' = \pi - \delta$ and the remaining points are distributed according to the scheme given by (2.19*a*). The points $\theta = 0$ and $\theta = \pi$ in the above procedure are replaced by the points $\theta = \delta$ and $\theta = \pi - \delta$, respectively, in order to eliminate the singular behaviour of the final coefficient matrix in the set of linear algebraic equations. Furthermore, in the vicinity of the two poles and near the discontinuity $\theta = \gamma$, an uneven point

distribution is prescribed in order to improve the accuracy of the results. On the orifice wall, S_{w^-}, N collocation points are chosen according to the distribution

$$R_i = \left[\frac{i-3}{N-1}\right]^3 (R_u - b) + b \quad (i = 1, 2, 3, \ldots, N), \tag{2.19b}$$

where R_u is a large positive number which defines the truncated domain ($b \leqslant R \leqslant R_u$) instead of the infinite domain ($b \leqslant R \leqslant \infty$). Numerical tests have demonstrated that it is sufficient to set $R_u = 20Z_0$ in order to achieve acceptable accuracy (Yan 1985).

In order to replace the integral equations with a set of algebraic equations it is first necessary to rewrite the unknown functions in terms of the appropriate coordinates. On the solid cap surface

$$f_1^{(b)}(\boldsymbol{x}) = -[T_{rr}(\theta)\sin\theta + T_{r\theta}(\theta)\cos\theta]\cos\phi, \tag{2.20a}$$

$$f_2^{(b)}(\boldsymbol{x}) = -[T_{rr}(\theta)\sin\theta + T_{r\theta}(\theta)\cos\theta]\sin\phi, \tag{2.20b}$$

$$f_3^{(b)}(\boldsymbol{x}) = -T_{rr}(\theta)\cos\theta + T_{r\theta}(\theta)\sin\theta. \tag{2.20c}$$

Similarly, on the clean surface of the bubble

$$T_{1r}^{(b)}[\boldsymbol{V}'(\boldsymbol{x})] = [t_{rr}(\theta)\sin\theta + t_{r\theta}(\theta)\cos\theta]\cos\phi, \tag{2.21a}$$

$$T_{2r}^{(b)}[\boldsymbol{V}'(\boldsymbol{x})] = [t_{rr}(\theta)\sin\theta + t_{r\theta}(\theta)\cos\theta]\sin\phi, \tag{2.21b}$$

$$T_{3r}^{(b)}[\boldsymbol{V}'(\boldsymbol{x})] = t_{rr}(\theta)\cos\theta - t_{r\theta}(\theta)\sin\theta; \tag{2.21c}$$

$$V_1'(\boldsymbol{x}) = [-U\sin\theta\cos\theta - V_R^s(\theta)]\cos\phi + V_\theta'(\theta)\cos\theta\cos\phi, \tag{2.22a}$$

$$V_2'(\boldsymbol{x}) = [-U\cos\theta\sin\theta - V_R^s(\theta)]\sin\phi + V_\theta'(\theta)\cos\theta\sin\phi, \tag{2.22b}$$

$$V_3'(\boldsymbol{x}) = -U\cos^2\theta - V_Z^s(\theta) - V_\theta'(\theta)\sin\theta. \tag{2.22c}$$

Finally, on the orifice wall, S_{w^-}

$$f_1^{(w)}(\boldsymbol{x}) = f_R^{(w)}(R)\cos\tilde{\theta}, \quad f_2^{(w)}(\boldsymbol{x}) = f_R^{(w)}(R)\sin\tilde{\theta}, \quad f_3^{(w)}(\boldsymbol{x}) = f_Z^{(w)}(R). \tag{2.23a,b,c}$$

Consequently, the unknown functions in (2.20)–(2.23) that have to be determined are T_{rr} and $T_{r\theta}$ on the stagnant cap, t_{rr} and V_θ' on the clean bubble surface, and $f_R^{(w)}$ and $f_Z^{(w)}$ on the orifice wall. These functions are approximated by a piecewise quadratic polynomial along the corresponding boundary intervals, which are given by

$$\hat{\theta}_1 = 0, \quad \hat{\theta}_n = \tfrac{1}{2}(\theta_n + \theta_{n+1}) \quad \text{for } n = 2, 3, \ldots, L-2, \quad \hat{\theta}_{L-1} = \gamma \quad \text{on } S_b^{(1)}, \tag{2.24a}$$

$$\hat{\theta}_1' = \gamma, \quad \hat{\theta}_n' = \tfrac{1}{2}(\theta_n' + \theta_{n+1}') \quad \text{for } n = 2, 3, \ldots, M-2, \quad \hat{\theta}_{M-1}' = \pi \quad \text{on } S_b^{(2)}, \tag{2.24b}$$

$$\hat{R}_1 = b, \quad \hat{R}_n = \tfrac{1}{2}(R_n + R_{n+1}) \quad \text{for } n = 2, 3, \ldots, N-2, \quad \hat{R}_{N-1} = R_u \quad \text{on } S_{w^-}. \tag{2.24c}$$

Hence, the quadratic polynomial representation of T_{rr} is

$$\begin{aligned} T_{rr}(\theta) = {} & T_{rr}^{(n-1)}(A_1^{(n)}\cos^2\theta + B_1^{(n)}\cos\theta + C_1^{(n)}) \\ & + T_{rr}^{(n)}(A_2^{(n)}\cos^2\theta + B_2^{(n)}\cos\theta + C_2^{(n)}) \\ & + T_{rr}^{(n+1)}(A_3^{(n)}\cos^2\theta + B_3^{(n)}\cos\theta + C_3^{(n)}), \end{aligned} \tag{2.25}$$

where $T_{rr}^{(j)} = T_{rr}(\theta = \theta_j)$, and the interpolation coefficients $A_j^{(n)}$, $B_j^{(n)}$ and $C_j^{(n)}$ are evaluated from the condition that $T_{rr}(\theta) = T_{rr}^{(n)}$ at $\theta = \theta_n$. An analogous quadratic representation (2.25) is employed for the remaining unknown functions. For t_{rk} the interpolating coefficients are denoted by A_i', B_i' and C_i' $(i = 1, 2, 3)$, while for $f_k^{(w)}$ they are denoted by A_i'', B_i'' and C_i'', respectively. In the latter, the function is quadratic in R. The polynomial representation of the tangential stress on the bubble surface requires clarification since the exact solution of Sadhal & Johnson (1983) for uniform flow past a droplet with a surfactant cap demonstrates the presence of a weak singularity in the stress at the edge of the cap. The singularity at $\theta = \gamma$ behaves as $(\cos\theta - \cos\gamma)^{-\frac{1}{2}}$, and is similar to the rim singularity given by Collins (1963) and Dorrepaal, O'Neill & Ranger (1976) for the flow past a solid spherical cap. In these problems the singular behaviour is derived analytically from the solution of a set of dual series equations that represents mixed boundary conditions on a spherical surface. Clearly, an asymptotic representation of the tangential stress in this form in the vicinity of the cap rim, $\theta = \gamma$, can enhance the accuracy of the eventual computations. Nevertheless, the behaviour near the singularity at $\theta = \gamma$ can be approximated by a polynomial similar to the one given by (2.25). This representation is based on the series expansion given in Sadhal & Johnson (1983) in terms of the associated Legendre functions of integer degree and order -1. Although the series representation excludes the rim $\theta = \gamma$, the behaviour in the vicinity of $\theta = \gamma$ is approximated by the polynomial which can be interpreted as a truncated series. This approximation does not provide an accurate description of the stress at the edge of the cap. Still, a correct behaviour in its vicinity is not precluded since the computed numerical value of the discretized stress $T_{r\theta}^{(n)}$ is not restricted. Consequently, the total drag acting on the droplet, which represents the directional integration of the stress over the entire spherical surface, is impalpably influenced by this approximation. The drag convergence tests, discussed in §3, demonstrate sufficient convergence with increasing number of collocation points despite the fact that convergence of the local interfacial stress and velocity is not necessarily attained. The latter will require a considerable increase in collocation points, and will result in prohibitively long computation time.

Finally, the kernels in the integral boundary conditions (2.17) of the single and double layer potentials are redefined by the equations

$$-\int_{S_b^{(1)}} u_i^k(\boldsymbol{x},\boldsymbol{y}) f_k^{(b)}(\boldsymbol{y})\,\mathrm{d}S_y = \frac{1}{8\pi}\int_{S_b^{(1)}} \left\{\frac{\delta_{ik}}{r_{xy}} + \frac{(x_i - y_i)(x_k - y_k)}{r_{xy}^3}\right\} f_k^{(b)}(\boldsymbol{y})\,\mathrm{d}S_y$$

$$= -\frac{1}{8\pi}\int_0^{\gamma}\int_0^{2\pi} K_{i1}\, T_{rr}\,\mathrm{d}\bar{\phi}\,\mathrm{d}\bar{\theta} - \frac{1}{8\pi}\int_0^{\gamma}\int_0^{2\pi} H_{i1}\, T_{r\theta}\,\mathrm{d}\bar{\phi}\,\mathrm{d}\bar{\theta}; \quad (2.26a)$$

$$\int_{S_b^{(1)}} T_{ij}[u^k(\boldsymbol{x},\boldsymbol{y})]\, V_k'(y)\,\mathrm{d}S_y = -\frac{3}{4\pi}\int_{S_b^{(1)}} \frac{(x_i - y_i)(x_j - y_j)(x_k - y_k)}{r_{xy}^5} W_k(\boldsymbol{y})\, y_j\,\mathrm{d}S_y$$

$$= \frac{3}{4\pi}\int_0^{\gamma}\int_0^{2\pi} H_i'(\boldsymbol{W})\,\mathrm{d}\bar{\phi}\,\mathrm{d}\bar{\theta}; \quad (2.26b)$$

$$\int_{S_b^{(2)}} u_i^k(\boldsymbol{x},\boldsymbol{y}) T_{kr}^{(b)}[\boldsymbol{V}'(\boldsymbol{y})]\,\mathrm{d}S_y = \frac{1}{8\pi}\int_{S_b^{(2)}} \left\{\frac{\delta_{ik}}{r_{xy}} + \frac{(x_i - y_i)(x_k - y_k)}{r_{xy}^3}\right\} T_{kr}^{(b)}[\boldsymbol{V}'(\boldsymbol{y})]\,\mathrm{d}S_y$$

$$= -\frac{1}{8\pi}\int_{\gamma}^{0}\int_0^{2\pi} K_{i1}\, t_{rr}\,\mathrm{d}\bar{\phi}\,\mathrm{d}\bar{\theta} + \frac{1}{8\pi}\int_{\gamma}^{0}\int_0^{2\pi} H_{i1}\, t_{r\theta}\,\mathrm{d}\bar{\phi}\,\mathrm{d}\bar{\theta}; \quad (2.26c)$$

$$\int_{S_b^{(2)}} T_{ij}[u^k(\boldsymbol{x},\boldsymbol{y})]\, V'_k(\boldsymbol{y})\, \mathrm{d}S_y = -\frac{3}{4\pi}\int_{S_b^{(2)}} \frac{(x_i-y_i)(x_j-y_j)(x_k-y_k)}{r_{xy}^5} V'_k(\boldsymbol{y})\, y_j\, \mathrm{d}S_y$$

$$= \frac{3}{4\pi}\int_\gamma^0 \int_0^{2\pi} H'_i\, V'_\theta\, \mathrm{d}\bar{\phi}\, \mathrm{d}\bar{\theta} + \frac{3}{4\pi}\int_\gamma^0 \int_0^{2\pi} H'_i(\boldsymbol{V})\, \mathrm{d}\bar{\phi}\, \mathrm{d}\bar{\theta}; \quad (2.26d)$$

$$\int_{S_w^-} u_i^k(\boldsymbol{x},\boldsymbol{y}) f_k^{(w)}(\boldsymbol{y})\, \mathrm{d}S_y = \frac{1}{8\pi}\int_{S_w^-} \left\{\frac{\delta_{ik}}{r_{xy}} + \frac{(x_i-y_i)(x_k-y_k)}{r_{xy}^3}\right\} f_k^{(w)}(\boldsymbol{y})\, \mathrm{d}S_y$$

$$= \frac{1}{8\pi}\int_b^\infty \int_0^{2\pi} F_{iR} f_R\, \mathrm{d}\bar{\bar{\theta}}\, \bar{R}\, \mathrm{d}\bar{R} + \frac{1}{8\pi}\int_b^\infty \int_0^{2\pi} F_{iZ} f_Z\, \mathrm{d}\bar{\bar{\theta}}\, \bar{R}\, \mathrm{d}\bar{R}, \quad (2.26e)$$

where the overbar indicates the coordinates of point $\boldsymbol{y}$. The functions defined by K_{i1}, H_{i1}, $H'_i(\boldsymbol{W})$, H_i and $H'_i(\boldsymbol{V})$ are known functions of $\bar{\theta}$ and $\bar{\phi}$, while the functions F_{iR} and F_{iZ} are known functions of $\bar{R}$ and $\bar{\theta}$. The expressions for these functions, although straightforward, are excessively long and will not be given here (for more details see Yan 1985).

Application of the boundary conditions (2.17) using the definitions (2.25) and (2.26) provides the following algebraic equations:

$$-\frac{1}{4\pi}\sum_{n=2}^{L-1}\sum_{\alpha=1}^{3} T_{rr}^{(n-2+\alpha)} G_\theta^{n\alpha}(K_{i1},1,\theta) - \frac{1}{4\pi}\sum_{n=2}^{L-1}\sum_{\alpha=1}^{3} T_{r\theta}^{(n-2+\alpha)} G_\theta^{n\alpha}(H_{i1},1,\theta)$$

$$-\frac{1}{4\pi}\sum_{n=2}^{M-1}\sum_{\alpha=1}^{3} t_{rr}^{(n-2+\alpha)} G_\theta'^{n\alpha}(K_{i1},1,\theta) - \frac{3}{2\pi}\sum_{n=2}^{M-1}\sum_{\alpha=1}^{3} V_\theta'^{(n-2+\alpha)} G_\theta'^{n\alpha}(H_i,1,\theta)$$

$$-\frac{1}{4\pi}\sum_{n=2}^{N-1}\sum_{\alpha=1}^{3} f_R^{(n-2+\alpha)} G_R^{n\alpha}(F_{iR},R,Z) - \frac{1}{4\pi}\sum_{n=2}^{N-1}\sum_{\alpha=1}^{3} f_Z^{(n-2+\alpha)} G_R^{n\alpha}(F_{iZ},R,Z)$$

$$= W_i(\boldsymbol{x}) + \frac{3}{2\pi}[S'_{V_i}(1,\theta) + S_{W_i}(1,\theta)] + \frac{1}{4\pi} S'_{t_i}(1,\theta)$$

$$\text{when } \boldsymbol{x} = (1,\theta,0) = (R,0,Z) \in S_b^{(1)}, \quad i = 1 \text{ or } 3; \quad (2.27a)$$

$$-V'_\theta(\boldsymbol{x})\cos\theta - \frac{1}{4\pi}\sum_{n=2}^{L-1}\sum_{\alpha=1}^{3} T_{rr}^{(n-2+\alpha)} G_\theta^{n\alpha}(K_{11},1,\theta)$$

$$-\frac{1}{4\pi}\sum_{n=2}^{L-1}\sum_{\alpha=1}^{3} T_{r\theta}^{(n-2+\alpha)} G_\theta^{n\alpha}(H_{11},1,\theta) - \frac{1}{4\pi}\sum_{n=2}^{M-1}\sum_{\alpha=1}^{3} t_{rr}^{(n-2+\alpha)} G_\theta'^{n\alpha}(K_{11},1,\theta)$$

$$-\frac{3}{2\pi}\sum_{n=2}^{M-1}\sum_{\alpha=1}^{3} V_\theta'^{(n-2+\alpha)} G_\theta'^{n\alpha}(H_1,1,\theta) + \frac{1}{4\pi}\sum_{n=2}^{N-1}\sum_{\alpha=1}^{3} f_R^{(n-2+\alpha)} G_R^{n\alpha}(F_{1R},R,Z)$$

$$-\frac{1}{4\pi}\sum_{n=2}^{N-1}\sum_{\alpha=1}^{3} f_Z^{(n-2+\alpha)} G_R^{n\alpha}(F_{1Z},R,Z)$$

$$= -U\cos\theta\sin\theta - V_R^s(\boldsymbol{x}) + \frac{3}{2\pi}[S'_{V_1}(1,\theta) + S_{W_1}(1,\theta)] + \frac{1}{4\pi} S'_{t_1}(1,\theta)$$

$$\text{when } \boldsymbol{x} = (1,\theta,0) = (R,0,Z) \in S_b^{(2)}; \quad (2.27b)$$

$$-V'_\theta(\boldsymbol{x})\sin\theta-\frac{1}{4\pi}\sum_{n=2}^{L-1}\sum_{\alpha=1}^{3}T_{rr}^{(n-2+\alpha)}G_\theta^{n\alpha}(K_{31},1,\theta)$$

$$-\frac{1}{4\pi}\sum_{n=2}^{L-1}\sum_{\alpha=1}^{3}T_{r\theta}^{(n-2+\alpha)}G_\theta^{n\alpha}(H_{31},1,\theta)-\frac{1}{4\pi}\sum_{n=2}^{M-1}\sum_{\alpha=1}^{3}t_{rr}^{(n-2+\alpha)}G_\theta^{\prime n\alpha}(K_{31},1,\theta)$$

$$-\frac{3}{2\pi}\sum_{n=2}^{M-1}\sum_{\alpha=1}^{3}V_\theta^{\prime(n-2+\alpha)}G_\theta^{\prime n\alpha}(H_3,1,\theta)+\frac{1}{4\pi}\sum_{n=2}^{N-1}\sum_{\alpha=1}^{3}f_R^{(n-2+\alpha)}G_R^{n\alpha}(F_{3R},R,Z)$$

$$-\frac{1}{4\pi}\sum_{n=2}^{N-1}\sum_{\alpha=1}^{3}f_Z^{(n-2+\alpha)}G_R^{n\alpha}(F_{3Z},R,Z)$$

$$=-U\cos^2\theta-V_Z^{\mathrm{s}}(\boldsymbol{x})+\frac{3}{2\pi}[S'_{V_3}(1,\theta)+S_{W_3}(1,\theta)]+\frac{1}{4\pi}S'_{t_3}(1,\theta)$$

$$\text{when } \boldsymbol{x}=(1,\theta,0)=(R,0,Z)\in S_{\mathrm{b}}^{(2)}; \quad (2.27c)$$

$$-\frac{1}{4\pi}\sum_{n=2}^{L-1}\sum_{\alpha=1}^{3}T_{rr}^{(n-2+\alpha)}G_\theta^{n\alpha}(K_{i1},1,\theta)-\frac{1}{4\pi}\sum_{n=2}^{L-1}\sum_{\alpha=1}^{3}T_{r\theta}^{(n-2+\alpha)}G_\theta^{n\alpha}(H_{i1},1,\theta)$$

$$-\frac{1}{4\pi}\sum_{n=2}^{M-1}\sum_{\alpha=1}^{3}t_{rr}^{(n-2+\alpha)}G_\theta^{\prime n\alpha}(K_{i1},1,\theta)-\frac{3}{2\pi}\sum_{n=2}^{M-1}\sum_{\alpha=1}^{3}V_\theta^{\prime(n-2+\alpha)}G_\theta^{\prime n\alpha}(H_i,1,\theta)$$

$$-\frac{1}{4\pi}\sum_{n=2}^{N-1}\sum_{\alpha=1}^{3}f_R^{(n-2+\alpha)}G_R^{n\alpha}(F_{iR},R,0)-\frac{1}{4\pi}\sum_{n=2}^{N-1}\sum_{\alpha=1}^{3}f_Z^{(n-2+\alpha)}G_R^{n\alpha}(F_{iZ},R,0)$$

$$=\frac{3}{2\pi}[S'_{V_i}(r,\theta)+S_{W_i}(r,\theta)]+\frac{1}{4\pi}S'_{t_i}(r,\theta)$$

$$\text{when } \boldsymbol{x}=(r,\theta,0)=(R,0,0)\in S_{\mathrm{w}^-}, \quad i=1 \text{ or } 3, \quad (2.27d)$$

where

$$G_\theta^{n\alpha}(F_i,r,\theta)=A_\alpha^{(n)}S_\theta(F_i,3,r,\theta,\hat\theta_{n-1},\hat\theta_n)+B_\alpha^{(n)}S_\theta(F_i,2,r,\theta,\hat\theta_{n-1},\hat\theta_n)$$
$$+C_\alpha^{(n)}S_\theta(F_i,1,r,\theta,\hat\theta_{n-1},\hat\theta_n), \quad (2.28a)$$

$$G_\theta^{\prime n\alpha}(F_i,r,\theta)=A_\alpha^{\prime(n)}S_\theta(F_i,3,r,\theta,\hat\theta_{n-1},\hat\theta_n)+B_\alpha^{\prime(n)}S_\theta(F_i,2,r,\theta,\hat\theta_{n-1},\hat\theta_n)$$
$$+C_\alpha^{\prime(n)}S_\theta(F_i,1,r,\theta,\hat\theta_{n-1},\hat\theta_n), \quad (2.28b)$$

$$G_R^{n\alpha}(F_i,r,\theta)=A_\alpha^{\prime\prime(n)}S_R(F_i,3,R,Z,\hat R_{n-1},\hat R_n)+B_\alpha^{\prime\prime(n)}S_R(F_i,2,R,Z,\hat R_{n-1},\hat R_n)$$
$$+C_\alpha^{\prime\prime(n)}S_R(F_i,1,R,Z,\hat R_{n-1},\hat R_n); \quad (2.28c)$$

$$S_\theta(F_i,I,r,\theta,a,b)=\int_a^b\cos^{I-1}\bar\theta\int_0^{2\pi}F_i\,\mathrm{d}\bar\phi\,\mathrm{d}\bar\theta, \quad (2.29a)$$

$$S_R(F_i,I,R,Z,a,b)=\int_a^b\bar R^I\theta\int_0^{2\pi}F_i\,\mathrm{d}\bar\phi\,\mathrm{d}\bar R, \quad (2.29b)$$

$$S_{W_i}(r,\theta)=\int_0^\gamma\int_0^{2\pi}H'_i(\boldsymbol{W})\,\mathrm{d}\bar\phi\,\mathrm{d}\bar\theta, \quad (2.29c)$$

$$S'_{V_i}(r,\theta)=\int_\gamma^\pi\int_0^{2\pi}H'_i(\boldsymbol{V})\,\mathrm{d}\bar\phi\,\mathrm{d}\bar\theta, \quad (2.29d)$$

$$S'_{t_i}(r,\theta)=\int_\gamma^\pi\int_0^{2\pi}H_{i1}\,t_{r\theta}\,\mathrm{d}\bar\phi\,\mathrm{d}\bar\theta. \quad (2.29e)$$

When (2.27) are applied at $(L+M+N)$ points on the system boundaries, they provide $I = 2(L+M+N)$ linear algebraic equations which can be solved for I unknowns; L unknown values of $T_{rr}^{(n)}$ and $T_{r\theta}^{(n)}$ $(n = 1, \ldots, L)$, M unknowns of $t_{rr}^{(n)}$ and V_θ' $(n = 1, \ldots, M)$, and N unknowns of $f_R^{(n)}$ and $f_Z^{(n)}$ $(n = 1, \ldots, N)$. The equations are solved using a standard Gaussian elimination method with complete pivoting. The most tedious part of this procedure is the evaluation of the integrals in (2.27). The integration with respect to $\bar{\phi}$ can be expressed analytically in terms of elliptic integrals of the first and second kind. The integration with respect to $\bar{\theta}$ is then carried out numerically (Yan *et al.* 1986).

3. The drag force on the bubble

The evaluation of the drag force acting on the bubble in the presence of the solid cap is determined from the equation

$$\begin{aligned} F_Z = &\int_{S_b^{(1)}} T_{rr}(\theta)\cos\theta\,\mathrm{d}S_y - \int_{S_b^{(1)}} T_{r\theta}(\theta)\sin\theta\,\mathrm{d}S_y \\ &+ \int_{S_b^{(2)}} t_{rr}(\theta)\cos\theta\,\mathrm{d}S_y - \int_{S_b^{(1)}} T_{j3}^{s}(\boldsymbol{y})\,n_j(\boldsymbol{y})\,\mathrm{d}S_y \\ &+ \int_{S_b^{(2)}} T_{rr}^{s}(\boldsymbol{y})\cos\theta\,\mathrm{d}S_y \end{aligned} \tag{3.1}$$

where $\mathrm{d}S_y = \sin\theta\,\mathrm{d}\theta\,\mathrm{d}\phi$. With the piecewise quadratic interpolation the first three integrals are performed analytically, while the last two are performed numerically with the stresses T_{ij}^{s} given from the Sampson solution for the flow through an orifice in the absence of the bubble. The calculated drag is scaled by the reference drag F_{Z_0} for the motion of a bubble with a stagnant cap in an infinite medium. The latter is given by the exact solution of Sadhal & Johnson (1983)

$$F_{Z_0} = U_c(4\pi + 2\gamma + \sin\gamma - \sin 2\gamma - \tfrac{1}{3}\sin 3\gamma), \tag{3.2}$$

where $U_c = U$ when the bubble is translating at constant velocity in quiescent fluid, and

$$U_c = \frac{3q}{2\pi b^2}\frac{b^2}{b^2+Z_0^2} = \frac{P_{-\infty}-P_\infty}{2\pi}\frac{b^3}{b^2+Z_0^2} \tag{3.3}$$

when the sphere is held at a fixed distance from the wall Z_0 in the presence of a pressure-gradient-driven flow into the orifice. Equation (3.3), in this case, is the Sampson velocity at the bubble centre in the absence of the bubble. Consequently, the ratio $\lambda = F_Z/F_{Z_0}$ will be presented for (i) a bubble moving away from the orifice in quiescent fluid, λ_t, and (ii) a fixed bubble in the presence of Sampson flow towards the orifice, λ_s.

Before applying the solution procedure many convergence tests have been carried out. In these tests the number of collocation points on each surface was gradually increased until the result for the drag correction factor, λ_t or λ_s, did not change up to the third significant digit. A summary of the selected values of L, M and N for different cap angles and all bubble-to-orifice spacings is given in table 1.

A comparison between the present results and the results obtained by Dagan *et al.* (1982) for the axisymmetric motion of a solid sphere near an orifice is shown in tables 2 and 3. The latter has employed the boundary collocation technique on the sphere boundary, while the no-slip boundary conditions on the orifice wall have been

	L		M		N	
γ						
0	0	0	25	30	20	20
0.5	13	13	25	25	20	20
1.0	15	15	20	20	20	20
1.5	20	20	20	20	20	20
2.0	21	21	25	25	20	20
2.5	25	25	9	9	20	20
π	25	25	0	0	20	20

TABLE 1. Selection of boundary collocation points (first column corresponds to a translating bubble, while the second corresponds to a fixed bubble in Sampson flow)

Z_0		$a/b = 0.1$	$a/b = 0.5$	$a/b = 1$	$a/b = 10$
10	(*a*)	−1.086	−1.124	−1.125	−1.126
	(*b*)	−1.060	−1.124	−1.126	−1.126
5	(*a*)	−1.084	−1.260	−1.280	−1.284
	(*b*)	−1.053	−1.251	−1.280	−1.285
3	(*a*)	−1.070	−1.404	−1.530	−1.568
	(*b*)	−1.051	−1.358	−1.517	−1.569
2	(*a*)	−1.061	−1.488	−1.871	−2.123
	(*b*)	−1.051	−1.392	−1.806	−2.125

TABLE 2. Comparison of F_z/F_{z_0} for a translating solid sphere; (*a*) present results, (*b*) Dagan *et al.* (1982. (a/b = bubble-to-pore radius ratio.)

Z_0		$a/b = 0.1$	$a/b = 0.5$	$a/b = 1$	$a/b = 10$
10	(*a*)	1.094	1.132	1.133	1.133
	(*b*)	1.056	1.119	1.120	1.121
5	(*a*)	1.100	1.299	1.312	1.323
	(*b*)	1.047	1.231	1.264	1.270
3	(*a*)	1.091	1.516	1.669	1.717
	(*b*)	1.044	1.292	1.479	1.560
2	(*a*)	1.084	1.697	2.223	2.671
	(*b*)	1.044	1.254	1.638	2.267

TABLE 3. Comparison of F_z/F_{z_0} for a stationary solid sphere in Sampson flow; (*a*) present results, (*b*) Dagan *et al.* (1982)

satisfied analytically. Hence, in principle, the results of Dagan *et al.* (1982) should be more accurate. A similar solution by Davis (1983) was obtained for a Stokeslet which can represent the motion of a small solid sphere with an accuracy of the order of $(a/b)^3$. Yan *et al.* (1986) have used a combined integral technique and multiple series representation whereby a collocation technique was utilized to satisfy the boundary conditions on the sphere surface while the integral representation accounted for the presence of the orifice wall (a comparison between the results of Dagan *et al.* (1982), Davis (1983) and Yan *et al.* (1986) is given in the latter).

For most cases considered in the comparison the present results differ from the results of Dagan *et al.* (1982) by one to few percent except for large spheres close to the orifice in Sampson flow. A similar accuracy was attained in the computations of Yan *et al.* (1986), which is a typical accuracy for the integral-equation method in general. The results of Davis (1983) are comparable with the present results for small spheres ($a/b < 1$) but their accuracy deteriorates when the sphere radius is increased. The difficulty in obtaining accurate results when the sphere is large compared with the orifice diameter and close to it in Sampson flow stems from the fact that for such conditions the flow field, and the consequential stress tensor, can possess steep gradients which requires a substantial increase in the number of collocation points.

The drag correction coefficients, for the two cases considered, are shown in figures 2 and 3. Figure 2 shows λ_t which represents the ratio of the drag in the presence of the orifice to the drag acting on the bubble with a stagnant cap in unbounded medium. The coefficient is described as a function of bubble-to-orifice distance, Z_0, and cap angle, γ. For cap angle $\gamma = \pi$, the results correspond to the drag acting on a solid sphere, which is higher than the drag acting on a clean bubble with $\gamma = 0$. The effect of bubble-to-orifice distance exhibits the strong hydrodynamic interaction when $Z_0 < 5$ with diminishing effect as the spacing is increased. In the limit of large spacing the drag is shown to approach the solution of Sadhal & Johnson (1983) for the unbounded problem ($\lambda \to 1$). The influence of the cap angle appears to be critical at $\gamma \approx \frac{1}{2}\pi$ rad, where the drag increases sharply from the low value associated with the clean bubble to the solid-sphere results. This effect is more pronounced at small bubble-to-orifice distance and it decreases with increasing spacing. The behaviour is clearly indicative of the large shear stresses at the trailing surface of the bubble. A similar behaviour is shown in figure 3 for λ_s which corresponds to the drag correction factor for Sampson flow towards an orifice in the presence of a bubble in a fixed position. Here, the effect of cap angle appears to be critical when $\gamma \approx \frac{3}{2}\pi$ although the increase in drag is not as steep as in the first case.

The terminal velocity of a bubble rising away from the orifice in the presence of flow into the pore can now be obtained by requiring a zero net force on the bubble. Using the result of Sadhal & Johnson as a characteristic velocity the force balance on the bubble can be written in the form

$$U_b \lambda_t + U_c \lambda_s = 1. \tag{3.4}$$

Consequently, the bubble velocity U_b is given by

$$U_b = (1 - U_c \lambda_s)/\lambda_t. \tag{3.5}$$

Hence, the bubble will remain in a fixed position when $U_c = 1/\lambda_s$, it will rise when $\lambda_s U_c < 1$ and approach the orifice when $\lambda_s U_c > 1$. The direction of motion is determined, therefore, by the conditions imposed by Sampson flow towards the orifice, while the magnitude of the bubble velocity is further influenced by the hydrodynamic interaction coefficient λ_t which can reduce substantially the rate of bubble rise in the vicinity of the orifice wall. Finally, in the absence of Sampson flow the bubble will rise at the rate

$$U_b = 1/\lambda_t. \tag{3.6}$$

It should be noted that for the case where Sampson flow is prescribed in the same direction as the bubble motion, the problem cannot be treated by the present model because the surfactant concentration is unknown and the stagnant-cap geometry

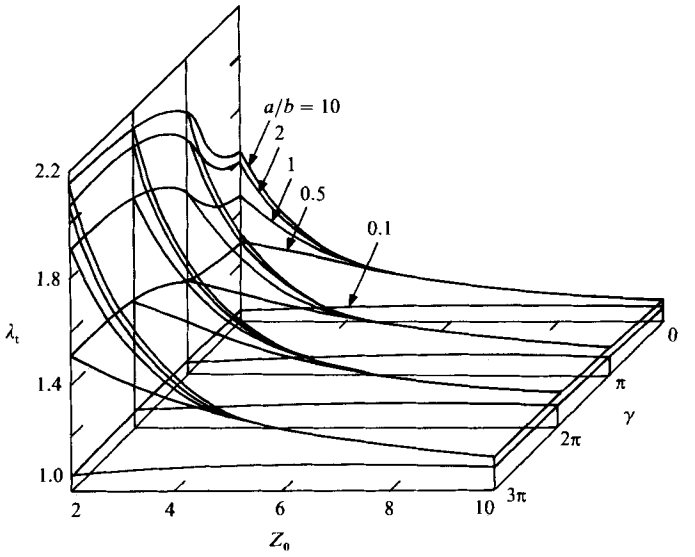

FIGURE 2. Drag correction factor, λ_t, for a bubble translating axisymmetrically away from the orifice.

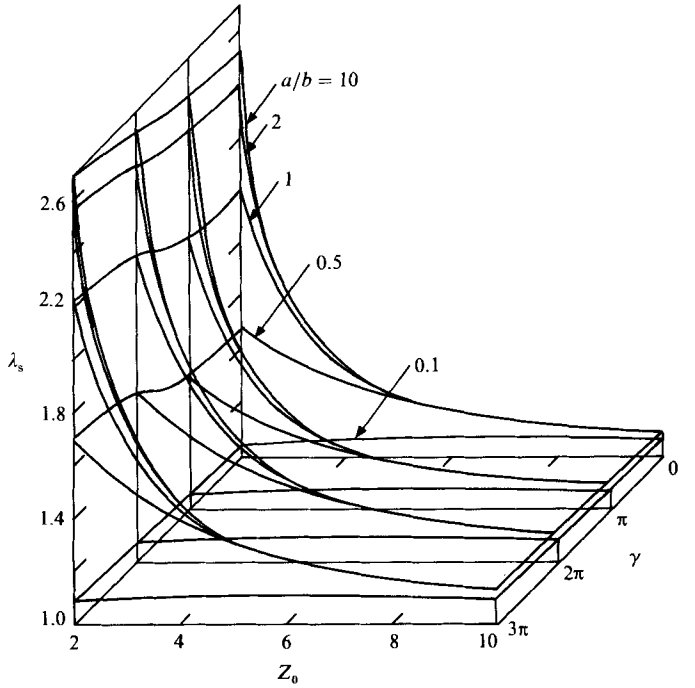

FIGURE 3. Drag correction factor, λ_s, for Sampson flow over a fixed bubble.

cannot be determined *a priori*. In this case the governing equations are coupled, and the surfactant concentration has to be obtained from the solution itself.

4. The stagnant cap

The significance of the results presented in §3 can be greatly enhanced by determining the way the cap angle changes with distance from the orifice for a

prescribed amount of surfactants on the bubble surface. Following the analysis of Sadhal & Johnson (1983) the difference between the maximum surface tension of the clean interface and the minimum tension at the trailing stagnation point can be obtained from the integration of the linear relations

$$\frac{\partial \sigma}{\partial \theta} = \tau_{r\theta} \quad \text{on } S_b^{(1)}. \tag{4.1}$$

Defining the inverse of the capillary number C_a, as the difference between $\sigma(\gamma)$ and $\sigma(0)$, (4.1) yields

$$C_a^{-1} = \int_0^{\gamma} \tau_{r\theta}\, \mathrm{d}\theta, \tag{4.2a}$$

where

$$\tau_{r\theta} = T_{r\theta}' + \tau_{r\theta}^{s}. \tag{4.2b}$$

Making use of the piecewise quadratic interpolation as shown in (2.25), the integration of $T_{r\theta}'$ can be performed analytically and (4.2) becomes

$$\begin{aligned} C_a^{-1} = {} & \int_0^{\gamma} \left(\cos\theta \frac{\partial V_R^s}{\partial r} - \sin\theta \frac{\partial V_Z^s}{\partial r} + \sin\theta \frac{\partial V_R^s}{\partial \theta} + \cos\theta \frac{\partial V_Z^s}{\partial \theta} \right) \mathrm{d}\theta \\ & + \sum_{n=2}^{L-1} \sum_{\alpha=1}^{3} T_{r\theta}^{(n-2+\alpha)} \{ \tfrac{1}{2} A_\alpha'' [\hat{\theta}_{n+1} - \hat{\theta}_n + \tfrac{1}{2}(\sin 2\hat{\theta}_{n+1} - \sin 2\hat{\theta}_n)] \\ & + B_\alpha''(\sin\hat{\theta}_{n+1} - \sin\hat{\theta}_n) + C_\alpha''(\hat{\theta}_{n+1} - \hat{\theta}_n) \}. \end{aligned} \tag{4.3}$$

The remaining integral in (4.3) was evaluated numerically, and the results are presented in figures 4 and 5. Figure 4 shows the results for the axisymmetric translation of the bubble in otherwise quiescent fluid. For small bubble radius ($a/b = 0.1$) the behaviour approaches the exact solution of Sadhal & Johnson with a maximum deviation of about 7% at $\gamma = \pi$, which corresponds to a solid sphere. This deviation is partly due to the inherent inaccuracy of the numerical technique, and, in addition, due to the finite distance between the bubble and the orifice. Furthermore, the results for a small bubble coalesce into a single curve (within 3%) for all the distances considered, $2 \leqslant Z_0 \leqslant 10$, which indicates minimal influence of the orifice wall on the bubble motion. For larger bubbles, C_a^{-1} increases with increasing bubble radius and diminishing bubble-to-orifice spacing. Hence, in the vicinity of the orifice, a larger surfactant concentration is required to establish the same cap angle as in the unbounded motion. Similar behaviour is demonstrated in figure 5 for a fixed bubble in Sampson flow into the orifice. Here, the magnitude of the inverse capillary number is smaller owing to the decreasing fluid velocity with distance from the orifice. Moreover, figure 5 is given for a fixed flow rate corresponding to $P_{-\infty} - P_{\infty} = 1$. Different flow rates will result in directly proportional changes of the inverse capillary number.

Some of the results shown in figures 4 and 5 indicate that the reciprocal capillary number attains a maximum value when the cap angle is about 2.7 rad. This behaviour is consistent for geometries involving bubbles equal to or larger than the pore and in its proximity ($Z_0 \leqslant 3$). Although the decrease in C_a^{-1} with increasing cap angle is small, this trend differs qualitatively from the monotonic behaviour associated with uniform flow past a capped bubble. In this context it should be emphasized that the presence of maxima in C_a^{-1} does not correspond to maximum drag. As shown in figures 2 and 3, the total drag increases monotonically with increasing cap angle, which is due to the combined contributions of the integrated

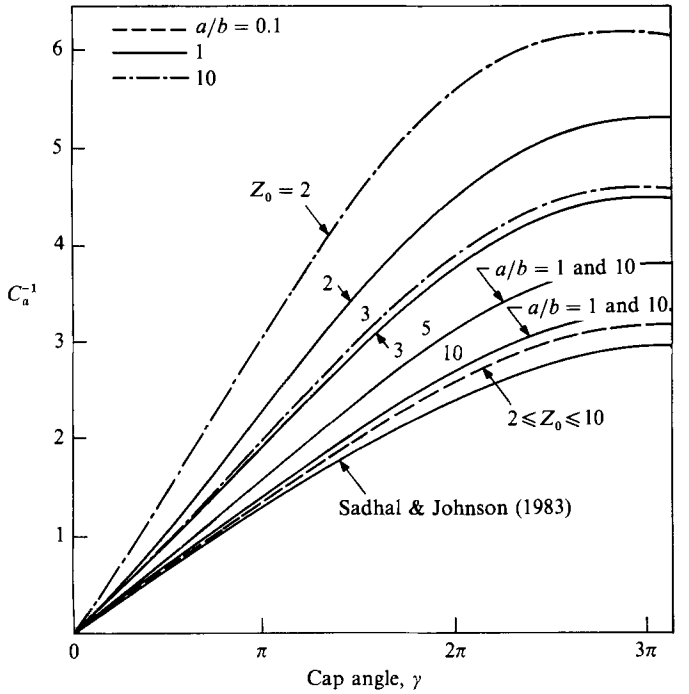

FIGURE 4. Reciprocal capillary number as a function of the cap angle for a bubble translating away from the orifice.

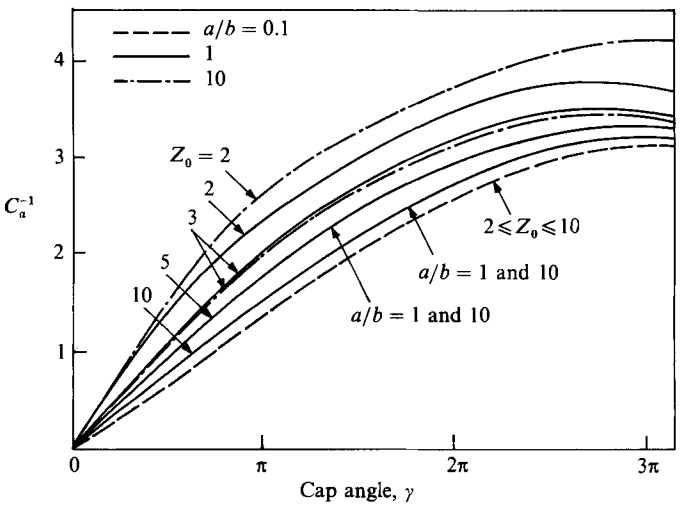

FIGURE 5. Reciprocal capillary number as a function of the cap angle for a fixed bubble in Sampson flow.

tangential and normal stress components on the spherical surface. The contribution of the normal stress to the total drag is, in principle, larger for the case involving flow through the orifice and exceeds that for uniform flow past a bubble due to the imposed pressure gradient in the exterior flow field ($P_{-\infty} > P_{\infty}$). The reciprocal capillary number, on the other hand, represents only the integral action of the shear stress on the immobile cap. Clearly, the total surface shear stress is influenced by the

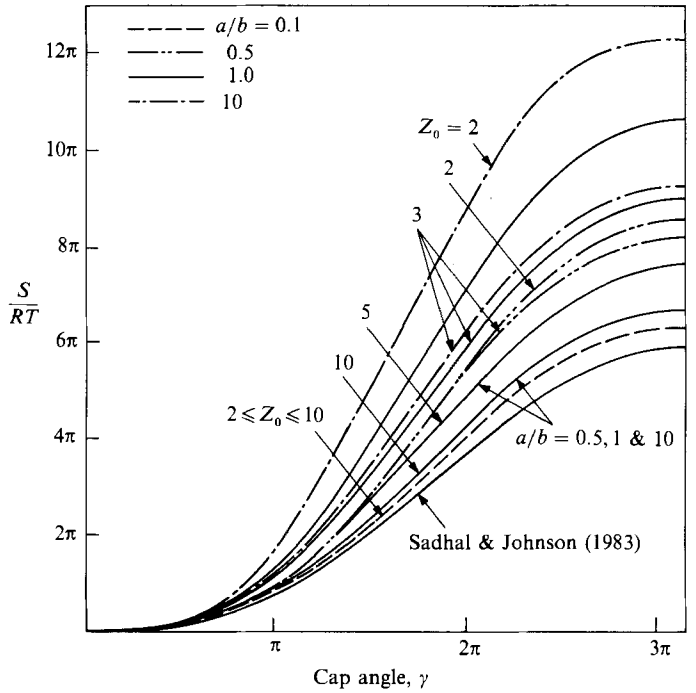

FIGURE 6. Total amount of surfactant on a bubble translation away from the orifice.

size of the immobile cap as well as by the magnitude of the local shear stress. The latter is a manifestation of the flow field in the vicinity of the cap. It is likely, therefore, to be expected that there will be larger local stresses when the bubble is close to the orifice boundary whereby the narrow gap between the spherical and wall boundaries introduces steep variations in the velocity field, and, consequently, larger tangential stresses. With increasing cap size, the immobile surface near the front stagnation point can act to retard the tangential velocity downstream along the spherical surface, and, therefore, reduce the magnitude of the local shear stress. Thus, the competing influences of the increase of the total shear stress for larger immobile surface and the accompanying reduction in the magnitude of the local stress can result in maximum C_a^{-1} when $\gamma < \pi$.

The monotonic decrease of the inverse capillary number with distance from the orifice for a fixed bubble size and cap angle indicates that for a constant amount of surfactants on the bubble surface the cap angle must expand as the bubble moves away from the orifice. To illustrate this effect the total amount of surfactants is computed using the Gibbs monolayer constitutive relations

$$\frac{\partial \sigma}{\partial \theta} = -RT\frac{\partial \Gamma}{\partial \theta}, \tag{4.4}$$

where T is the temperature and R is the universal gas constant. Clearly, the ideal monolayer description given by (4.4) is not necessarily suitable for the stagnant interface, which can be characterized as a condensed film and, therefore, does not obey the linear gaseous relations. Nevertheless, the linear Gibbs relations can provide

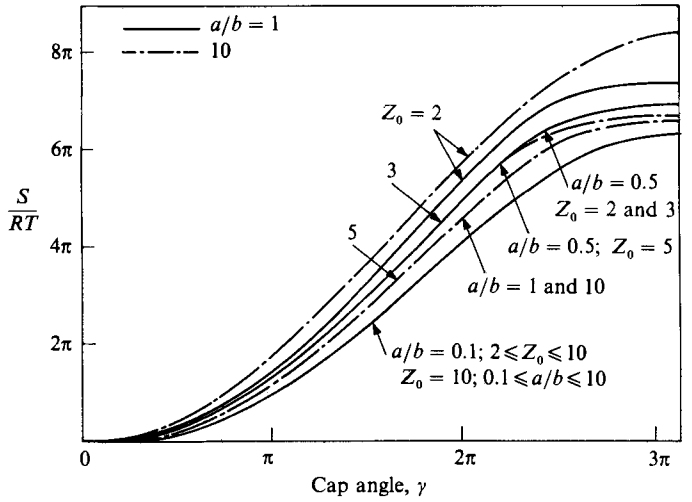

FIGURE 7. Total amount of surfactants on a fixed bubble in Sampson flow.

a useful qualitative description of the stagnant-cap expansion. Consequently, the total amount of surfactants can be determined from the relation

$$S = 2\pi \int_0^{\gamma} \Gamma(\theta) \sin\theta \, \mathrm{d}\theta = \frac{2\pi}{RT} \int_0^{\gamma} [\sigma_{\max} - \sigma(\theta)] \sin\theta \, \mathrm{d}\theta. \tag{4.5}$$

Using a similar quadratic interpolation as shown in (4.3), equation (4.5) was integrated numerically and the results are shown in figures 6 and 7. For the case of a translating bubble (figure 6). The exact solution of Sadhal & Johnson is approached for small bubble size, $a/b = 0.1$, with an accuracy of less than 7%. For larger bubbles and smaller bubble-to-orifice spacing the total amount of surfactants exceeds appreciably the values associated with the unbounded solution. Therefore, for a constant amount of surfactants, the stagnant-cap angle increases with distance from the orifice until the entire bubble surface becomes immobile. The expanding cap results in a monotonic increase of the drag correction factor, λ_t, while the diminishing hydrodynamic interaction reduces the drag. The combined effect enhances the influence of the orifice boundary on the motion of the bubble, and, consequently, the decrease of the drag with distance is slower than the behaviour indicated by figure 2 for a constant cap angle. The same qualitative behaviour is shown in figure 7 for a fixed bubble in Sampson flow. Here, the presence of the bubble in the vicinity of the orifice exposes the interface to increasing external currents which act to condense the cap and reduce its angle. In the case of a bubble rising from the orifice in the presence of Sampson flow, the two cases can be combined linearly to obtain the dynamic cap size evolution and the corresponding drag correction factor.

5. Conclusions

The motion of a bubble at the exit of an orifice, in the presence of flow in the opposite direction, is shown to be greatly influenced by the hydrodynamic interaction with the confining boundary and by the presence of a stagnant cap of insoluble surfactants. The results demonstrate that for a fixed amount of surfactants on the

bubble surface the size of the stagnant cap will increase with increasing distance from the orifice owing to the decreasing sweeping effect of the exterior phase. Consequently, the area of the immobile surface increases and the drag-force decrease is slower when compared to a constant-cap-size bubble. The present results compare well with the exact solution of Sadhal & Johnson (1983) for the translation of a bubble in the presence of a stagnant cap in unbounded medium. Furthermore, a comparison with the numerical collocation solution of Dagan *et al.* (1982) for the axisymmetric motion of a solid sphere in the vicinity of an orifice shows good agreement. The numerical inaccuracy associated with the present results is estimated to be smaller than 7%, which is typical of the numerical integral technique employed in this study.

The main shortcoming of the present solution is that it does not consider the effect of bubble deformation. Sadhal & Johnson (1986) have shown that in unbounded flow the shape of the bubble is close to a prolate spheroid and the deformation is cap-size dependent. For small stagnant caps the downstream interface exhibits larger deformations than the front surface, while the behaviour is reversed for large cap angles. Moreover, the influence of the confining orifice wall will enhance such deformation at close bubble-to-orifice spacing.

The numerical boundary-integral technique employed in this study appears to be useful for treating problems involving complicated geometry although it is restricted by its limited accuracy and long computation time. The average computation time required to evaluate the drag force for a single configuration and prescribed flow conditions is about 5 minutes of CPU time on an IBM 3081 computer. Furthermore, despite the acceptable convergence of the total drag the local distributions of the stress components and the interfacial velocity do not converge with sufficient accuracy. Therefore, the computation of the streamlines cannot be performed unless the number of collocation points is considerably increased which, in turn, will require prohibitively long computation time.

Finally, it is important to emphasize that the present analysis is based on an *priori* determination of the stagnant-cap location. Other interesting cases, associated with the motion of a bubble near the orifice in the presence of insoluble surfactants, can arise when the motion of the bubble coincides with the direction of the exterior flow. When the bubble rises from the orifice and the flow is in the same direction a stagnant belt of surfactants can be formed owing to the directional change of the interfacial velocity. On the other hand, when both the exterior fluid and the bubble move towards the orifice two stagnant caps on the bubble poles can be established. In both cases the problem can be treated, in principle, by the present technique with a two-variable iterative trial and error procedure where the belt location and its size, in the first case, or the sizes of the stagnant caps, in the second, are sought. Nevertheless, this method is restricted by the excessive computation time required to complete a single iterative run. It seems that an alternative procedure in which the coupled hydrodynamic and mass conservation equations are considered simultaneously is preferable (Holbrook & Levan 1983*a*, *b*).

This work was supported by the National Science Foundation Grant number CPE-8404261.

REFERENCES

Argawal, S. K. & Wasan, D. T. 1979 *Chem. Engng Sci.* **18**, 215.

Beitel, A. & Heideger, W. J. 1971 *Chem. Engng Sci.* **26**, 711.

COLLINS, W. D. 1961 *Proc. Camb. Phil. Soc.* **57**, 367.

COLLINS, W. D. 1963 *Mathematika* **10**, 72.

DAGAN, Z., WEINBAUM, S. & PFEFFER, R. 1982 *J. Fluid. Mech.* **115**, 505.

DAVIS, A. M. J. 1983 *Intl J. Multiphase Flow* **9**, 575.

DAVIS, R. & ACRIVOS, A. 1966 *Chem. Engng Sci.* **21**, 681.

DORREPAAL, J. M., O'NEILL, M. E. & RANGER, K. B. 1976 *J. Fluid Mech.* **75**, 273.

GARNER, F. H. & SKELLAND, A. H. P. 1955 *Chem. Engng Sci.* **4**, 149.

GRIFFITH, R. M. 1962 *Chem. Engng Sci.* **17**, 1057.

HAPPEL, J. & BRENNER, H. 1973 *Low Reynolds Number Hydrodynamics*. Noordhoff.

HARPER, J. F. 1973 *Adv. Appl. Mech.* **12**, 59.

HARPER, J. F. 1974 *Q. J. Mech. Appl. Maths* **27**, 87.

HARPER, J. F. 1982 *Appl. Sci. Res.* **38**, 343.

HETSRONI, G. 1982 *Handbook of Multiphase Systems*. McGraw-Hill.

HOLBROOK, J. A. & LEVAN, M. D. 1983*a* *Chem. Engng Commun.* **20**, 191.

HOLBROOK, J. A. & LEVAN, M. D. 1983*b* *Chem. Engng Commun.* **20**, 273.

HORTON, T. J., FRITSCH, T. R. & KINTNER, R. C. 1965 *Can. J. Chem. Engng* **43**, 143.

HUANG, W. S. & KINTNER, R. C. 1969 *AIChE J.* **15**, 735.

JOHNS, L. E. & BECKMAN, R. B. 1966 *AIChE J.* **12**, 10.

LADYZHENSKAYA, O. A. 1963 *The Mathematical Theory of Viscous Incompressible Flow*, chap. 3. Gordon & Breach.

LEVAN, M. D. & NEWMAN, J. 1976 *AIChE J.* **22**, 695.

LEVICH, V. G. 1962 *Physicochemical Hydrodynamics*. Prentice-Hall.

NEWMAN, J. 1967 *Chem. Engng Sci.* **22**, 83.

SADHAL, S. S. & JOHNSON, R. E. 1983 *J. Fluid Mech.* **126**, 237.

SADHAL, S. S. & JOHNSON, R. E. 1986 *Chem. Engng Commun.* **46**, 97.

SAVIC, P. 1953 *Nat. Res. Counc. Can., Div. Mech. Engng Rep.* MT-22.

SAVILLE, D. A. 1973 *Chem. Engng J.* **5**, 251.

SCHECHTER, R. S. & FARELY, R. W. 1963 *Can. J. Chem. Engng* **41**, 103.

WASSERMAN, M. L. & SLATTERY, J.C. 1969 *AIChE J.* **15**, 533.

YAN, Z. 1985 Three-dimensional hydrodynamic and osmotic pore entrance phenomena. Ph.D. dissertation, The City University of New York.

YAN, Z., WEINBAUM, S., GANATOS, P. & PFEFFER, R. 1986 *J. Fluid Mech.* **174**, 39.